Marine Stratocumulus Convection. Part II: Horizontally Inhomogeneous Solutions

WAYNE H. SCHUBERT, JOSEPH S. WAKEFIELD, ELLEN J. STEINER AND STEPHEN K. COX

Department of Atmospheric Science, Colorado State University, Fort Collins 80523

(Manuscript received 29 July 1977, in final form 22 January 1979)

ABSTRACT

Solutions of the horizontally inhomogeneous version of the coupled, convective-radiative, cloud-topped mixed-layer model described in Part I of this study are presented. Both numerical and approximate analytical methods are used to investigate the downstream variations which occur as boundary-layer air flows through regions of varying sea surface temperature and large-scale divergence. Six numerical experiments are performed.

In the first two experiments boundary-layer air flows through regions of constant large-scale divergence but of increasing or decreasing sea surface temperature. In the cold advection case the boundary layer warms, moistens and deepens in time, while the turbulent fluxes increase. In the warm advection case the boundary layer cools, drys and becomes shallower, while the turbulent fluxes decrease. In addition the cloud base descends and there is a tendency to form a surface fog.

In the third and fourth experiments boundary-layer air flows through regions of constant sea surface temperature but of increasing or decreasing large-scale divergence. In these two integrations essentially no model variable changes except cloud top. Cloud top slowly rises if divergence is decreasing and slowing falls if divergence is increasing. The adjustment time for cloud top is long and thus the boundary-layer depth may be far from its horizontally homogeneous steady-state value. The distinct difference between the adjustment time for the thermodynamic properties of the mixed layer and the adjustment time for cloud top is illustrated in a fifth experiment.

The sixth experiment simulates the wintertime flow of cold air off the Asian continent across the warm Kuroshio Current. Although the surface flux of water vapor is very large, the boundary-layer mixing ratio is fairly constant, i.e., the boundary layer deepens so rapidly in the downstream direction that the mixing of dry air across cloud top maintains a relatively dry boundary layer.

1. Introduction

In Part I of this study (Schubert *et al.*, 1979) we presented a coupled, convective-radiative, boundary-layer model of marine stratocumulus convection. Under horizontally homogeneous steady-state conditions the governing differential equations reduced to a system of algebraic equations which could be easily solved. Solutions were presented for various sea surface temperatures and large-scale divergences. In this paper we present solutions of the horizontally inhomogeneous version of the model, i.e., we present numerical and approximate analytical solutions of the system (3.31)–(3.43) of Part I, with the assumption that all radiative cooling appears as a discontinuity at cloud top. The numerical results are obtained using the procedure described in Section 3.3 of Part I.

We are concerned here with the variation of the dependent variables of the model under varying externally specified parameters, primarily varying sea surface temperature and large-scale divergence. The results presented here can be interpreted either in a Lagrangian sense (i.e., as the downstream modification following a parcel along its trajectory) or in a locally steady-state, horizontally inhomogeneous sense (i.e., assuming $\partial/\partial t = 0$ and interpreting the substantial derivative d/dt as $V\partial/\partial x$). To facilitate both interpretations, we have labeled figures with both distance and time.

Since our governing system contains three first-order differential equations, we must specify initial conditions on h_M, $(q + l)_M$ and z_B. In all cases we have initialized the model with the relevant steady-state, horizontally homogeneous solution. The only finite-differencing procedure needed for solution is a time-differencing scheme for the differential equations for h_M, $(q + l)_M$ and z_B. Because of its accuracy we have chosen to use the classical fourth-order Runge-Kutta scheme.

Table 1 outlines the sea surface temperature, wind speed and large-scale divergence used in the six experiments we shall discuss. The first four experiments are idealized situations which are based on the eastern North Pacific maps of Neiburger *et al.* (1961) and Miller and Stevenson (1974). The mean July maps of Neiburger *et al.* (Figs. 1–3) show resultant streamlines and isotachs, sea surface

0022-4928/79/071308-17$08.25

TABLE 1. Externally specified parameters for various model experiments. Experiments 1–5 use the mean July Oakland sounding for h_+, q_+ and $LW_+^{\downarrow}$. Experiment 6 uses a typical AMTEX sounding (see figure 5).

	Sea surface temperature T_S	Wind speed V (m s^{-1})	Divergence D
Experiment 1: Movement from cold to warm water with a constant divergence field.	T_S linearly increases from 15 to 20°C over 1000 km.	7	4×10^{-6} s^{-1}
Experiment 2: Movement from warm to cold water with a constant divergence field.	T_S linearly decreases from 16 to 14°C over 1000 km.	7	4×10^{-6} s^{-1}
Experiment 3: Movement from low divergence to high divergence with a constant sea surface temperature field.	15°C	7	D linearly increases from 2×10^{-6} s^{-1} to 6×10^{-6} s^{-1} over 1000 km.
Experiment 4: Movement from high divergence to low divergence with a constant sea surface temperature field.	15°C	7	D linearly decreases from 6×10^{-6} s^{-1} to 2×10^{-6} s^{-1} over 1000 km.
Experiment 5: Movement over a discontinuous 2°C increase in sea surface temperature.	T_S changes discontinuously from 14 to 16°C.	7	4×10^{-6} s^{-1}
Experiment 6: Simulation of a wintertime cold air outbreak over the East China Sea, 16 February 1975.	$T_S(x) = T_0 + \Delta T \tanh \times [(x - x_0)/d]$	12	10.2×10^{-6} s^{-1}

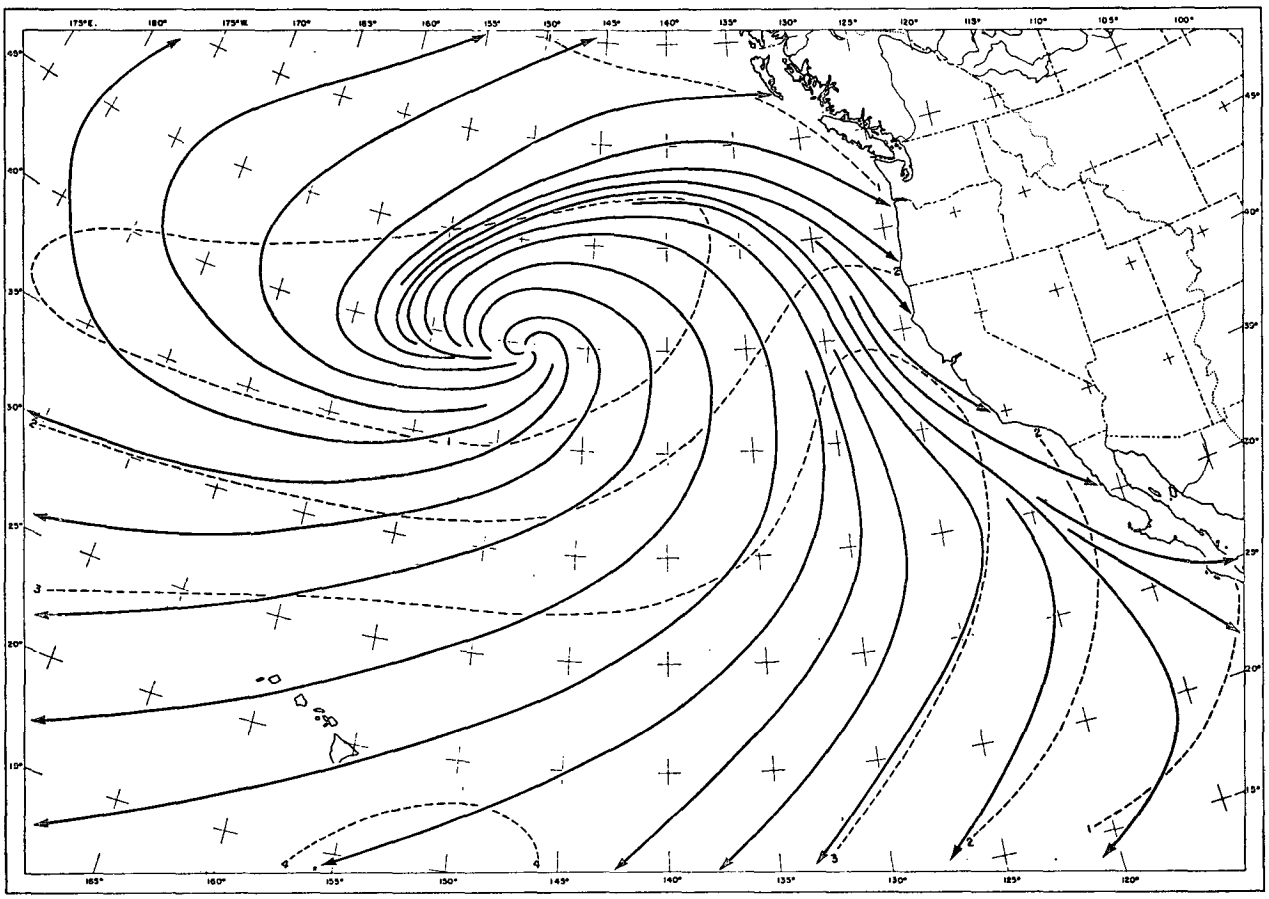

FIG. 1. Resultant surface wind streamlines and isotachs for July. After Neiburger *et al.* (1961).

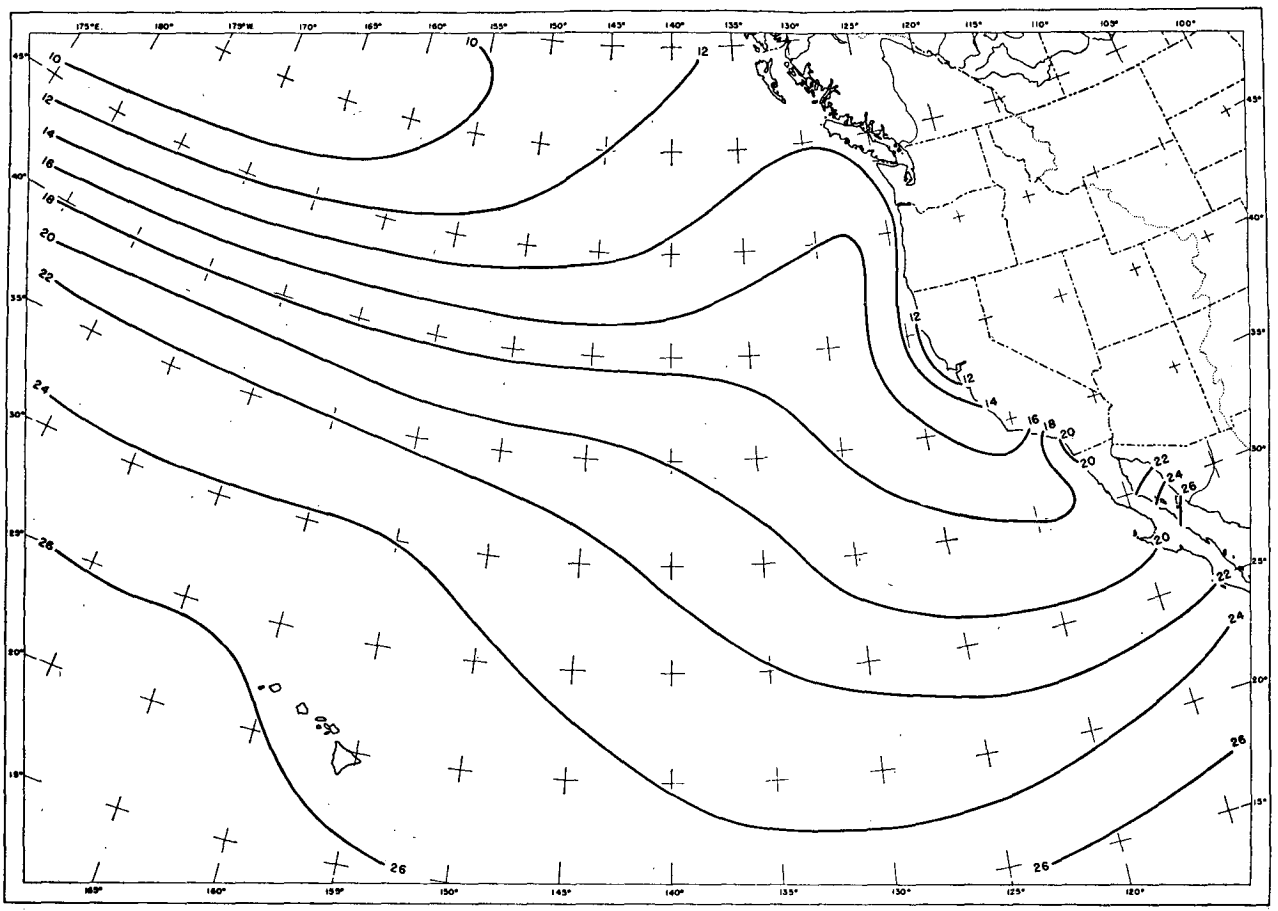

FIG. 2. Mean sea surface temperature for July (°C). After Neiburger *et al.* (1961).

temperature and large-scale divergence. One deficiency of Fig. 1 is that it displays resultant wind speed, i.e., the speed of the vector-averaged wind. What should probably be used for V in the model is the average wind speed. Miller and Stevenson's diagram of mean July 1961–74 surface pressure, resultant wind direction, resultant wind speed and average wind speed is shown in Fig. 4. Note the large differences between resultant wind speed and average wind speed. These maps indicate that there is a large region southwest of San Francisco where marine layer air passes from cold to warm sea surface temperature and from high to low divergence. The maps also indicate that there is a region northwest of San Francisco where the air passes from warm to cold sea surface temperature and from low to high divergence. Experiments 1–4 have been designed to isolate the influence of varying sea surface temperature and varying divergence in these two regions. Thus, we have used the mean July Oakland sounding to compute the linear functions h_+, q_+, and $\mathrm{LW}_+^{\downarrow}$ shown in Fig. 5.

Experiment 5 is an attempt to illustrate the different adjustment time for h_M and $(q + l)_M$ as opposed to that for z_B. In experiment 5 we have again used the mean Oakland sounding for h_+, q_+ and $\mathrm{LW}_+^{\downarrow}$.

Experiment 6 is an attempt to simulate the rapid changes which occur in a cold air outbreak over the Kuroshio Current. Our sea surface temperature pattern takes the form

$$T_S(x) = T_0 + \Delta T \tanh\frac{x - x_0}{d}, \qquad (1.1)$$

where we have chosen T_0 as 14°C, ΔT as 7°C, x_0 as 500 km and d as 70 km. Eq. (1.1) is an attempt to fit the mean February sea surface temperature pattern, assuming approximately northwesterly surface flow. The mean February pattern, along with the surface winds for 0000–0600 GMT 16 February 1975, is shown in Figs. 6a and 6b. The profiles of h_+, q_+ and $\mathrm{LW}_+^{\downarrow}$ shown in Fig. 5 are taken from the 0000 and 0600 GMT AMTEX soundings for 16 February 1975. A DMSP satellite image for 0255 GMT 16 February 1975 is shown in Fig. 6c.

The remainder of this paper is devoted to a discussion of these six experiments.

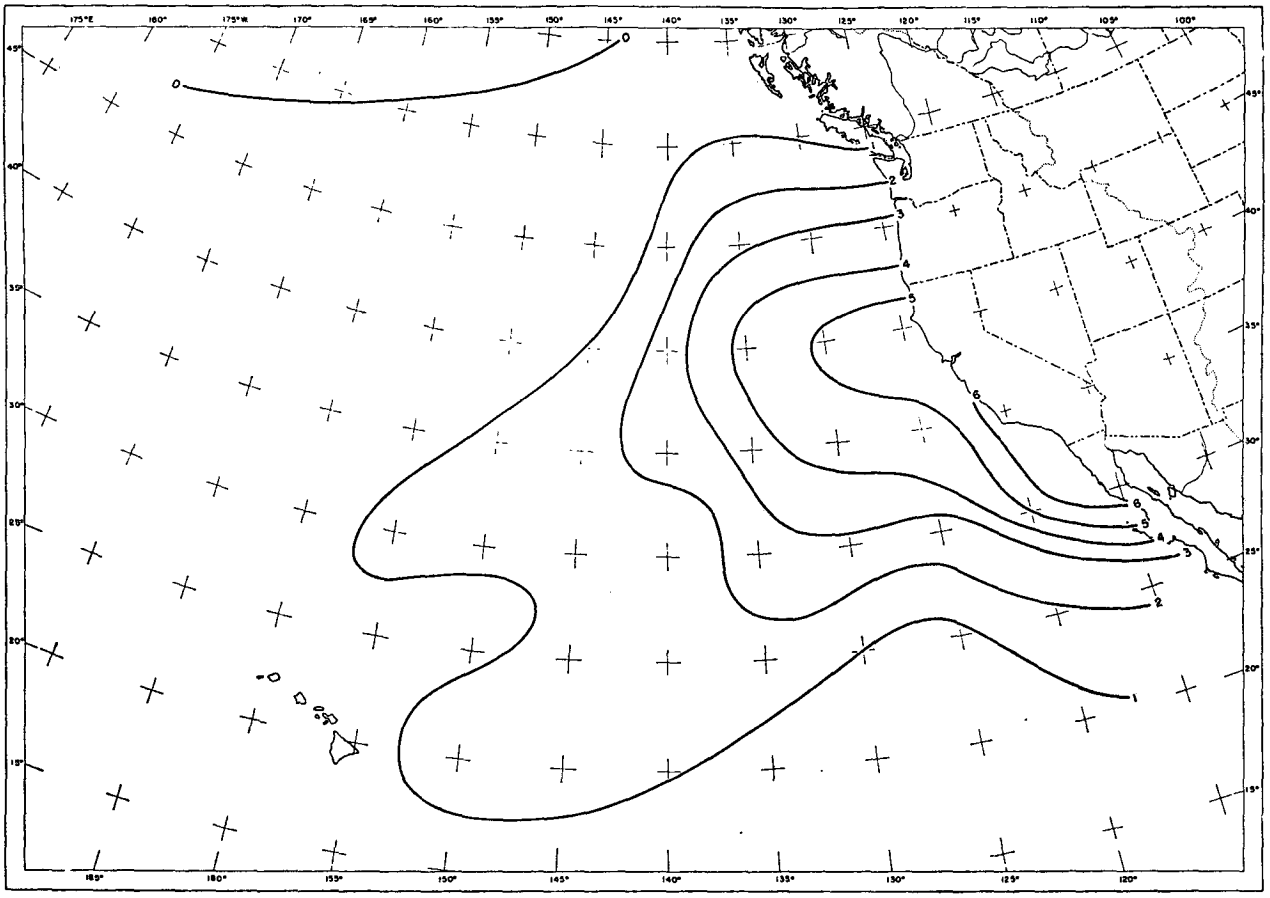

FIG. 3. Divergence of resultant surface winds for July (10^{-6} s^{-1}). After Neiburger *et al.* (1961).

2. Influence of varying sea surface temperature

The first two experiments are designed to illustrate mixed-layer behavior under conditions of constant wind speed (7 m s^{-1}), constant divergence (4×10^{-6} s^{-1}) and varying sea surface temperature. In Experiment 1 (Fig. 7) air moves along a trajectory toward warmer water, with the sea surface temperature gradient being 5°C (1000 km)$^{-1}$. In Experiment 2 (Fig. 8) air moves toward colder water, with the sea surface temperature gradient being −2°C (1000 km)$^{-1}$.

The results of Experiment 1 show that advection over warmer water produces increases in z_B, h_M, $(q + l)_M$, and the fluxes of h and $q + l$. In addition, the increase in h_M and $(q + l)_M$ is such that the subcloud layer is warmed enough for z_C to rise, even though the marine layer is moistening. The cold advection very quickly produces a positive $(\overline{w's'_v})_S$. After 500 km about 50% of the buoyant production of turbulent kinetic energy (Fig. 7f) is coming from the subcloud layer, while after 1000 km about 60% is coming from the subcloud layer. Some of the differences between Experiment 1 at 600 km or about 24 h and the steady-state, horizontally homogeneous solutions of Part I are shown in Table 2. As might be expected, in this cold advection situation the cloud top and cloud base tend to be lower, h_M and $(q + l)_M$ tend to be smaller, and the surface fluxes tend to be larger. But perhaps most interesting is the large difference in cloud-top heights. The cloud top after 600 km is only 515 m, which is considerably lower than the steady-state, horizontally homogeneous value of 872 m. We shall later attempt to explain this in terms of the slow adjustment time for z_B.

The results of Experiment 2 show that advection over colder water causes z_B, z_C, h_M, $(q + l)_M$, and the fluxes of h and $q + l$ to decrease. The descent of cloud base indicates a tendency to produce a fog at the surface. In two other experiments (not shown) in which we changed the sea surface temperature gradient from −2°C(1000 km)$^{-1}$ to −3°C(1000 km)$^{-1}$ and −4°C(1000 km)$^{-1}$ (leaving the initial conditions unchanged), cloud base descended to the surface in 990 and 570 km, respectively. Figs. 1 and 2 indicate that northwest of San Francisco summertime cold advective situations stronger than −4°C

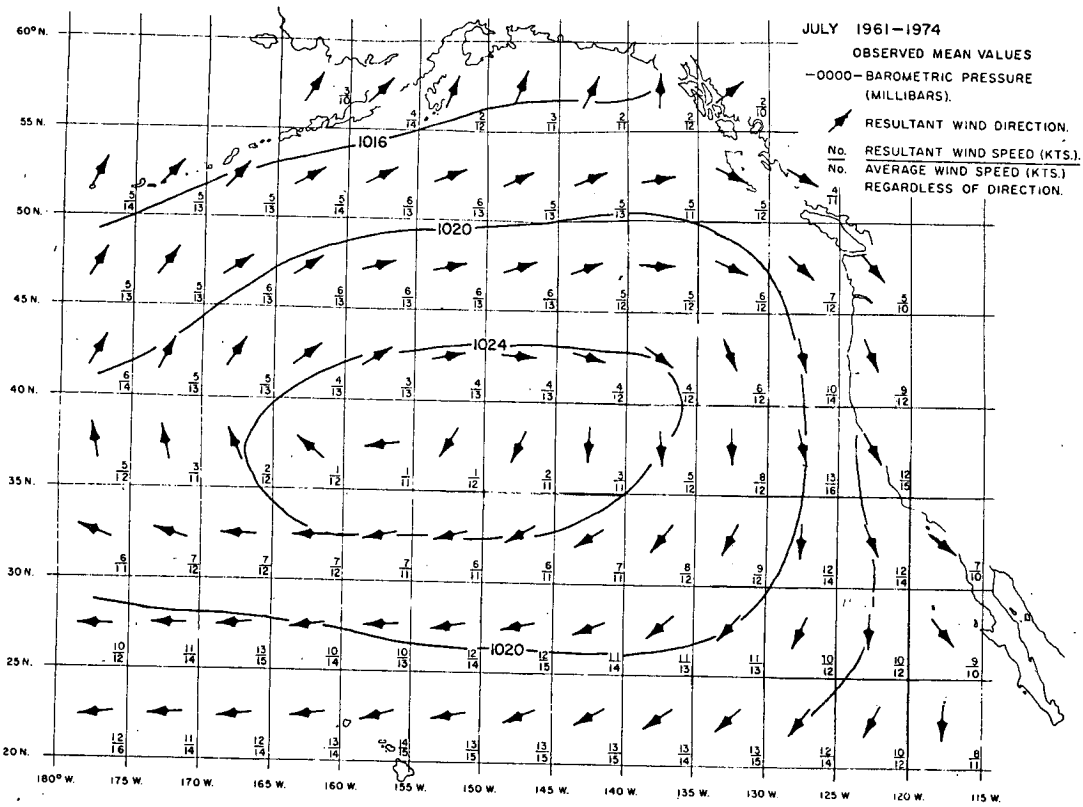

FIG. 4. Mean July (1961–74) surface pressure, resultant wind direction, resultant wind speed (numerator) and average wind speed (denominator). After Miller and Stevenson (1974).

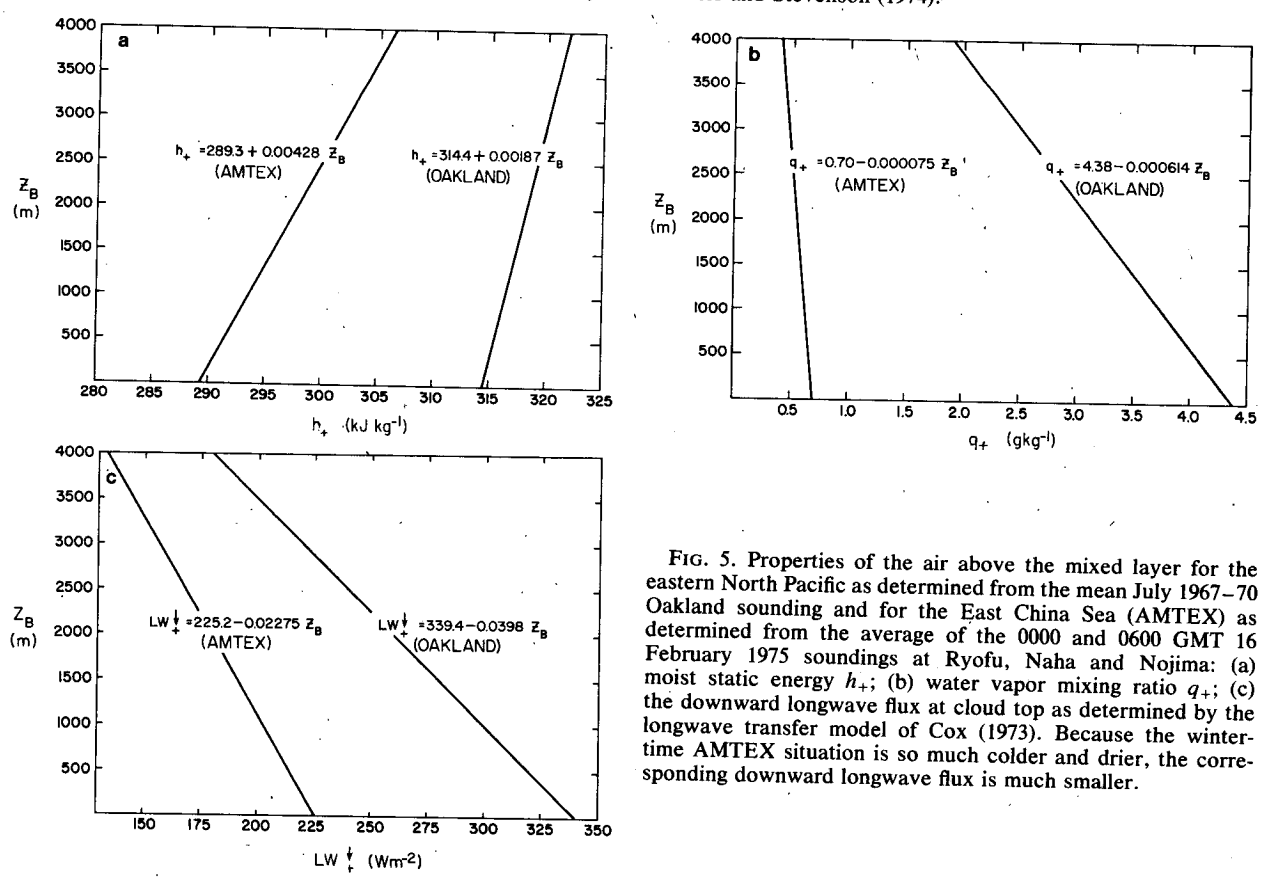

FIG. 5. Properties of the air above the mixed layer for the eastern North Pacific as determined from the mean July 1967–70 Oakland sounding and for the East China Sea (AMTEX) as determined from the average of the 0000 and 0600 GMT 16 February 1975 soundings at Ryofu, Naha and Nojima: (a) moist static energy h_+; (b) water vapor mixing ratio q_+; (c) the downward longwave flux at cloud top as determined by the longwave transfer model of Cox (1973). Because the wintertime AMTEX situation is so much colder and drier, the corresponding downward longwave flux is much smaller.

$\times$ (1000 km)$^{-1}$ are quite common. Thus, the northern California and southern Oregon coasts must be regions of frequent summertime fog. That this is indeed the case is illustrated in Table 3, which shows the average number of days with visibility less than a half-mile for coastal Oregon and California stations. The most interesting feature of the table is the summertime high incidence of low visibility in northern California as opposed to the low incidence in southern California.

3. Influence of varying large-scale divergence

Experiments 3 and 4 are designed to illustrate mixed-layer behavior under conditions of constant wind speed (7 m s^{-1}), constant sea surface temperature (15°C) and varying large-scale divergence. In Experiment 3 (Fig. 9) air moves toward higher divergence, with the gradient being 4×10^{-6} s^{-1} $\times$ (1000 km)$^{-1}$. In Experiment 4 (Fig. 10) air moves toward lower divergence with the gradient being -4×10^{-6} s^{-1}(1000 km)$^{-1}$.

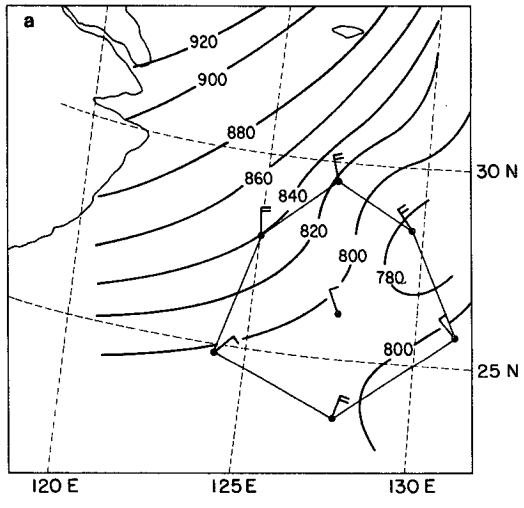

FIG. 6a. Horizontal distribution of the pressure (mb) at the inversion base at 0000 GMT 16 February 1975. After Ninomiya (1976). Also shown are the 0000–0600 GMT surface winds.

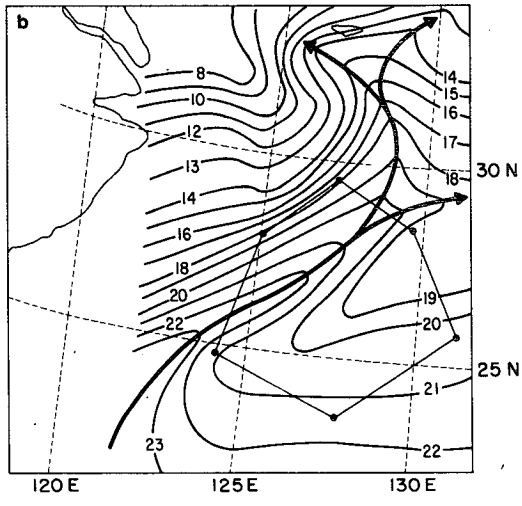

FIG. 6b. Position of the Kuroshio Current and the mean sea surface temperatures for February 1968 (from Lenschow, 1972). For present purposes this mean map can be regarded as identical to the AMTEX '75 map presented by the Japanese Oceanographic Group (1975).

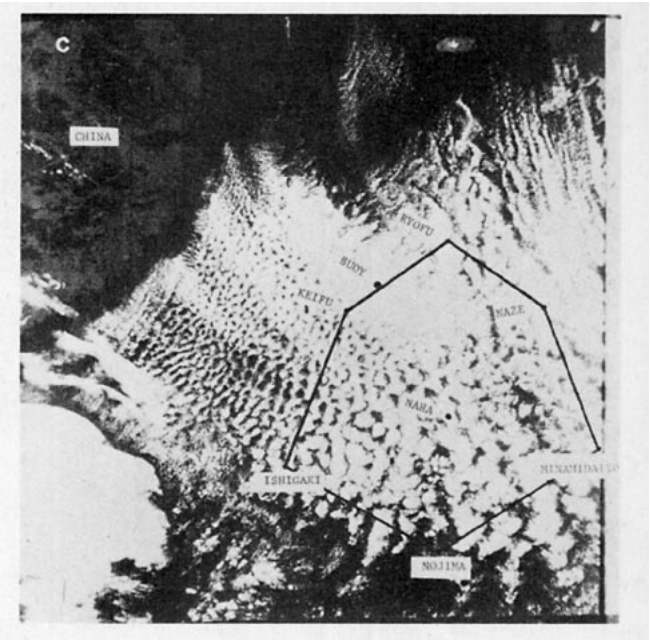

FIG. 6c. DMSP visible image taken at 0255 GMT 16 February 1975 showing extensive stratocumulus deck associated with a cold air outbreak. Also shown is the AMTEX hexagonal network. After Lenschow and Agee (1976).

A general feature of Experiments 3 and 4 is that for all practical purposes there is no variation of any model variable except z_B. Although it may at first sight seem surprising, this feature is consistent with Figs. 8–12 of Part I, which show that in the steady-state, horizontally homogeneous case, of the variables z_B, z_C, h_M, $(q + l)_M$, $\overline{w'h'}$ and $w'(\overline{q' + l'})$, only z_B has a strong dependence on divergence in the range 2×10^{-6} to 6×10^{-6} s^{-1}.

Another interesting feature of these two experiments is the slow adjustment of cloud top. If z_B after 1000 km in Experiment 3 were in a horizontally homogeneous steady state, it would be the same as the initial value of z_B in Experiment 4. Conversely, if z_B after 1000 km in Experiment 4 were in a horizontally homogeneous steady state, it would be the same as the initial value of z_B in Experiment 3. Thus, even in weak advective situations we might expect to find z_B rather far from its horizontally homogeneous steady-state value.

4. Adjustment times

In Experiment 5 (Fig. 11) mixed-layer air, after flowing for a long period over water with a temperature of 14°C, instantaneously encounters water of

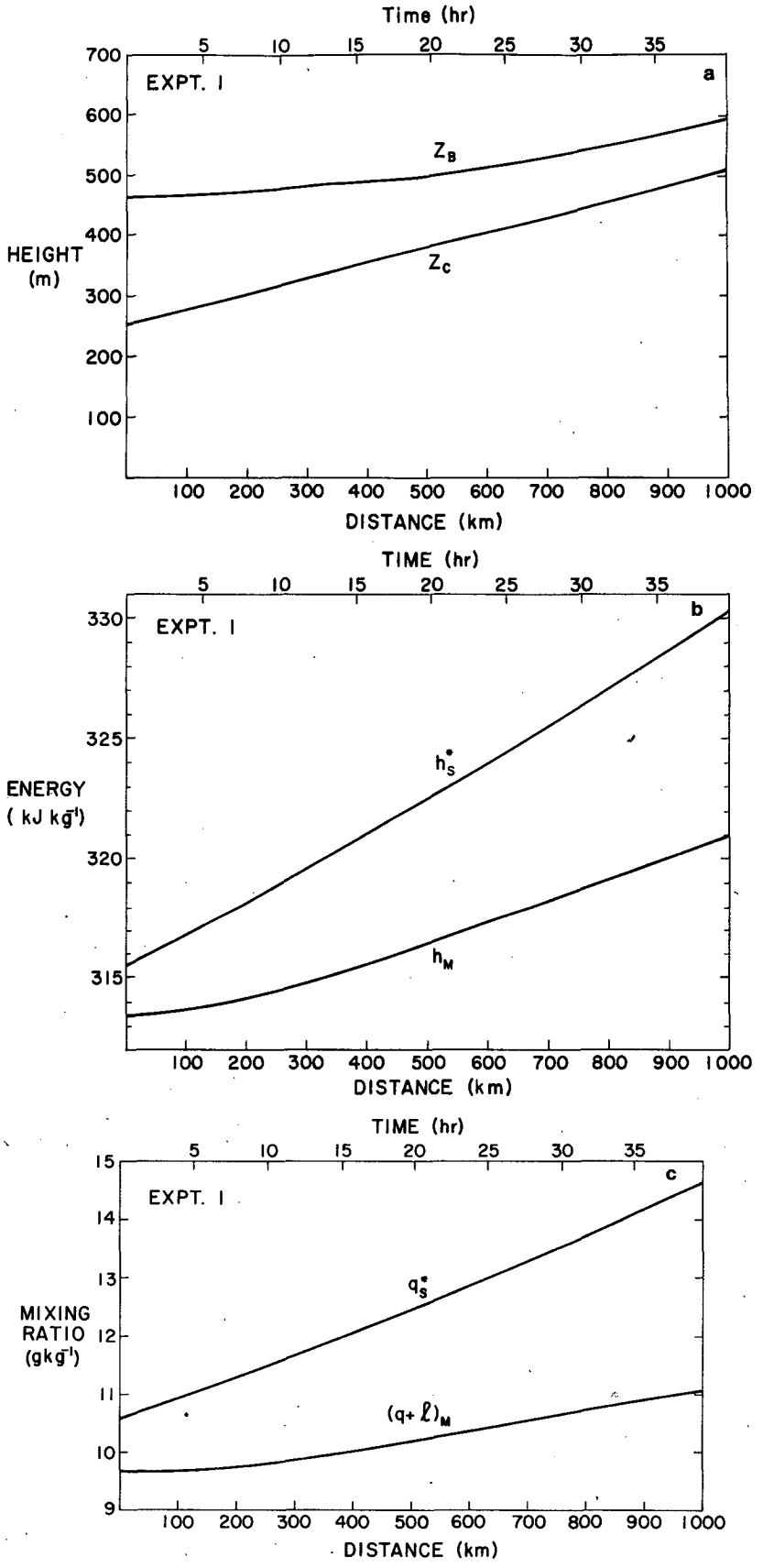

FIG. 7. Results for Experiment 1 (constant divergence, increasing sea surface temperature).

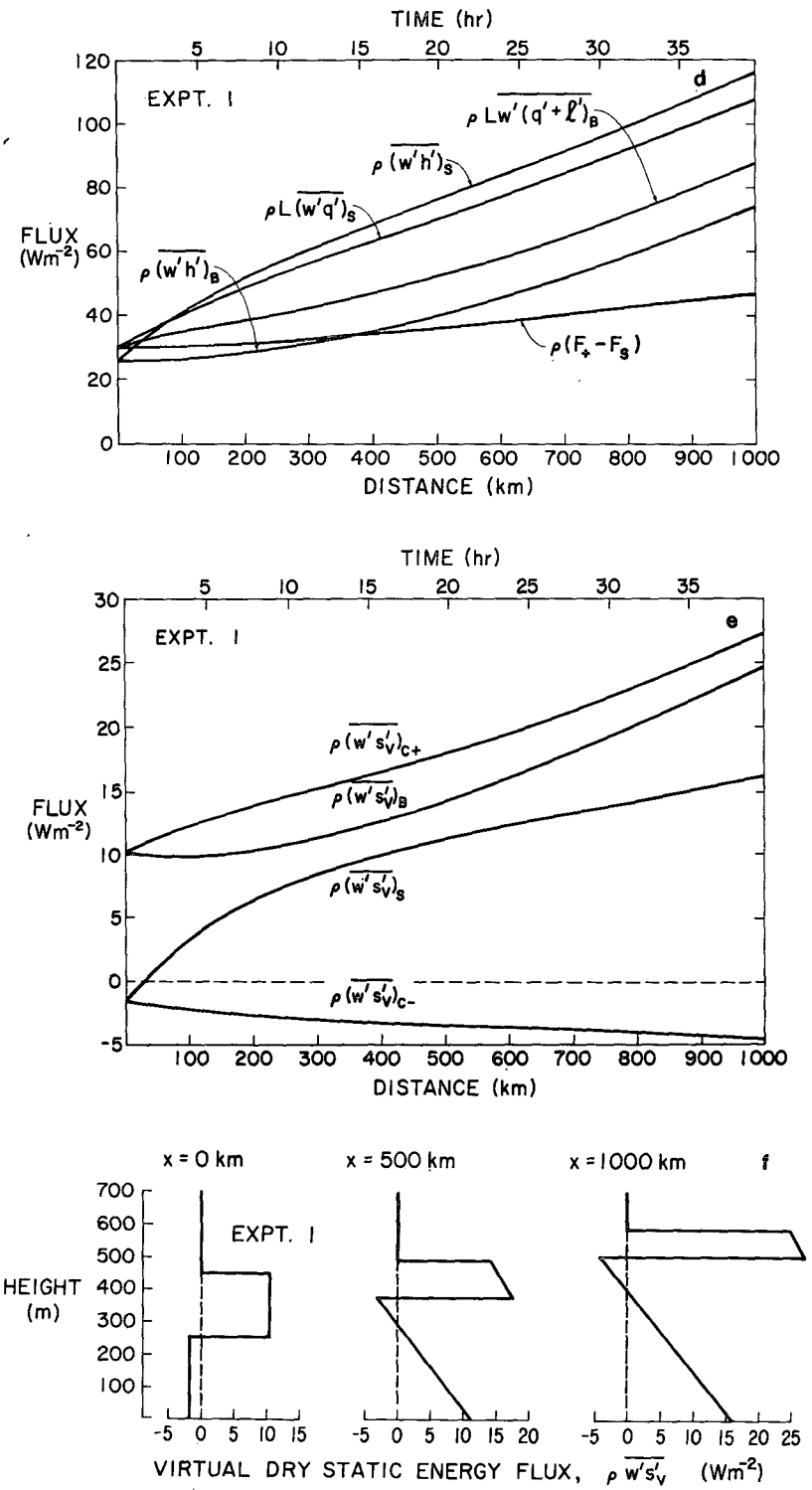

FIG. 7. (*Continued*)

16°C. As expected an adjustment to the new conditions occurs. Cloud top and cloud base become higher, h_M and $(q + l)_M$ increase, and the fluxes of h and $q + l$ adjust to nearly double their original values. For z_B to change 63% of the way to its asymptotic value requires 80 h, while for h_M and $(q + l)_M$ to change 63% of the way to their asymptotic values requires only 4 h. This large difference in

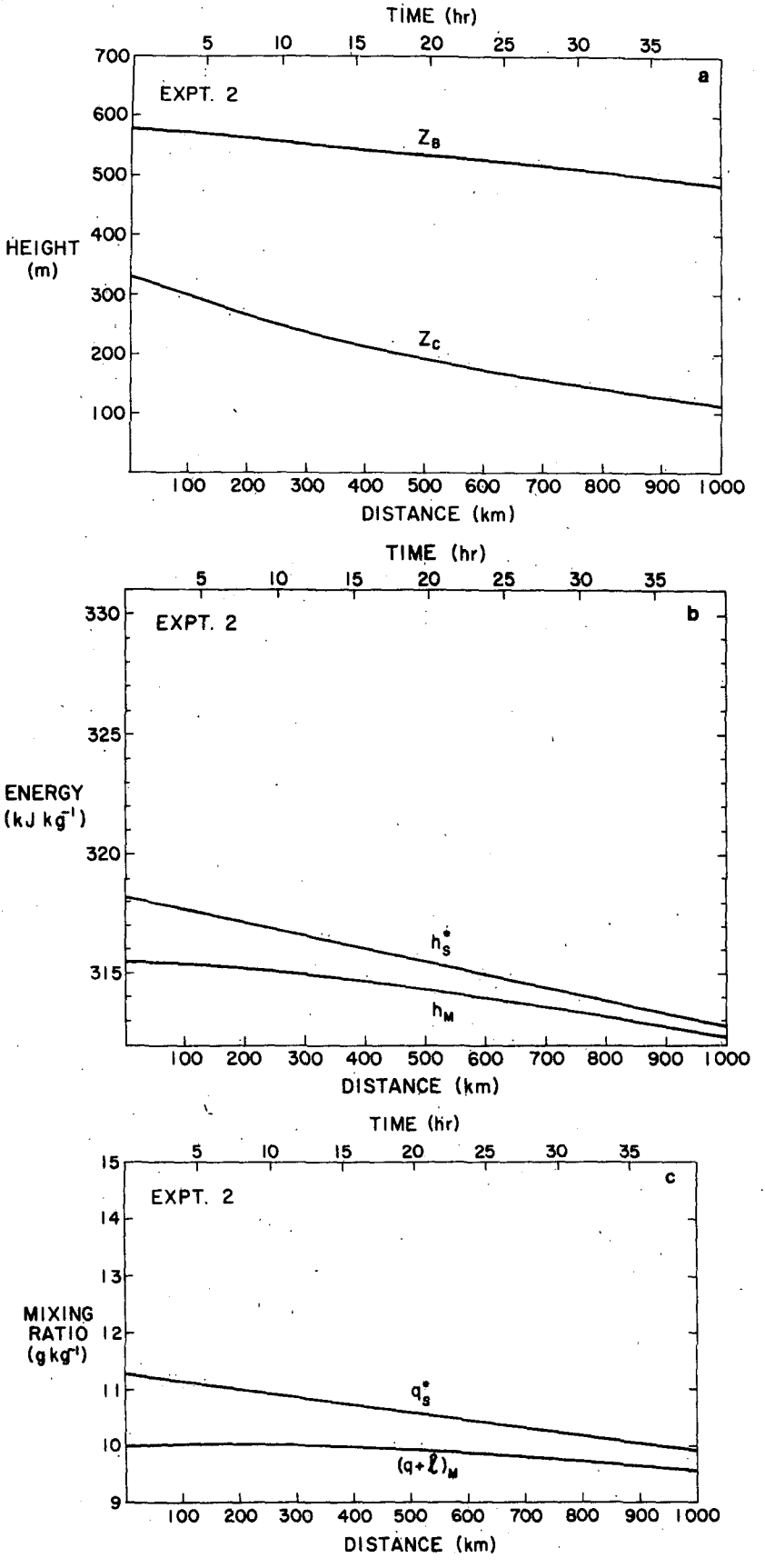

FIG. 8. Results for Experiment 2 (constant divergence, decreasing sea surface temperature).

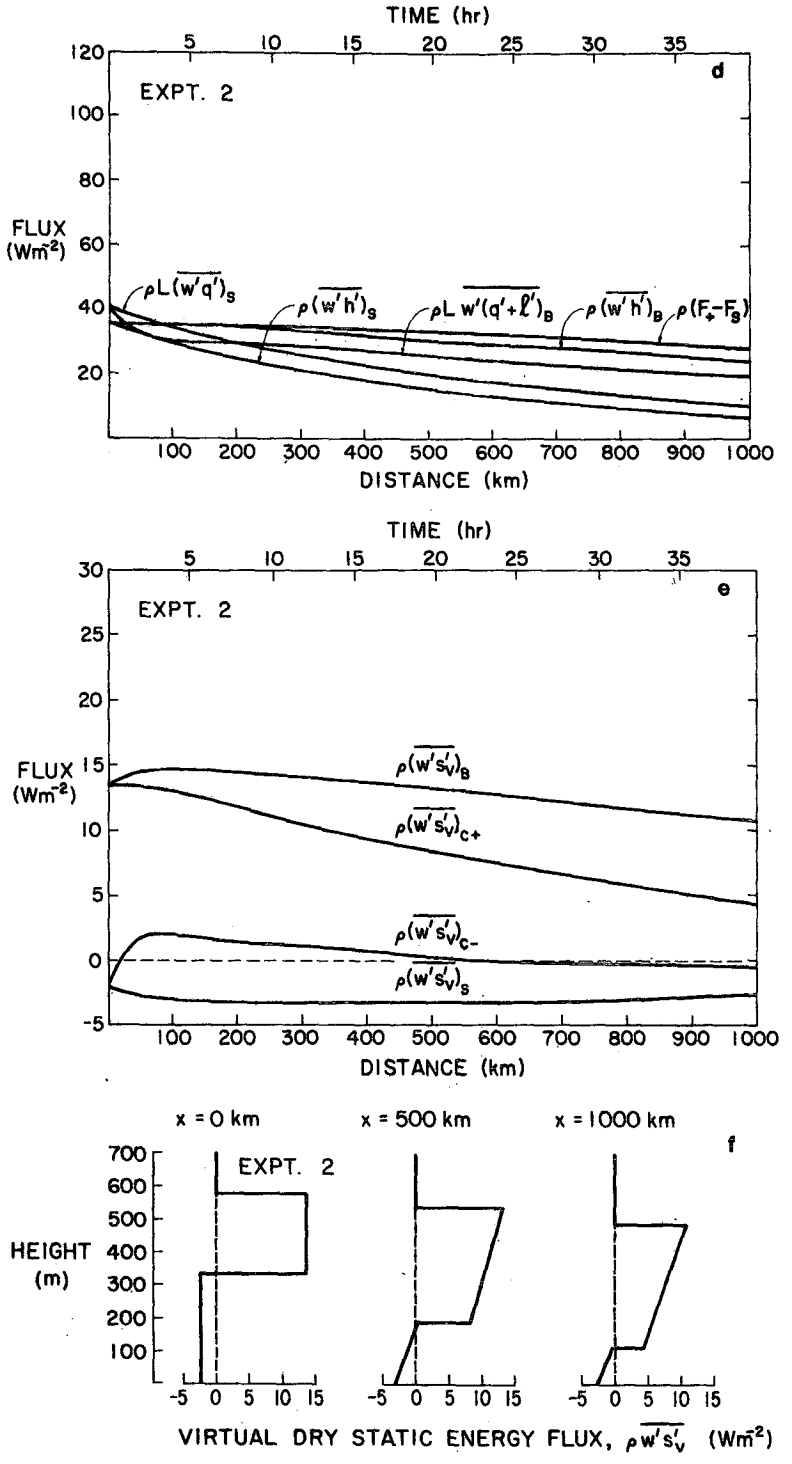

FIG. 8. (*Continued*)

the adjustment time for z_B as opposed to that for h_M and $(q + l)_M$ appears to be a general feature of the model under typical eastern ocean situations. We shall offer an explanation of this phenomenon in Section 6.

5. Wintertime air mass transformation

The gradients of sea surface temperature used in Experiments 1 and 2 are characteristic of marine stratocumulus of the eastern oceans. When winter-

TABLE 2. Comparison of the steady-state, horizontally inhomogeneous solution after 600 km (i.e., where T_S is 18°C) of Experiment 1 with the steady-state, horizontally homogeneous solution.

	Horizontally inhomogeneous	Horizontally homogeneous
z_B (m)	515	872
z_C (m)	405	511
h_M (kJ kg^{-1})	317.38	319.14
$(q + l)_M$ (g kg^{-1})	10.37	10.59
$\rho\overline{(w'h')_S}$ (W m^{-2})	83	60
$\rho L\overline{(w'q')_S}$ (W m^{-2})	76	69

TABLE 3. The average number of days on which there was at least one observation of visibility less than 0.5 mi. Data were compiled from U.S. Naval Weather Service (1969).

Station	Latitude (°N)	JFM	AMJ	JAS	OND	Year
Astoria	46.2	8.2	4.4	10.4	14.8	37.8
North Bend	43.4	10.4	11.7	29.0	24.7	75.8
Crescent City	41.8	7.0	14.8	38.1	19.7	79.6
Eureka	40.8	8.2	14.9	38.7	27.7	89.5
Monterey Peninsula	36.6	7.6	6.9	20.3	14.7	49.5
Los Angeles	33.9	13.1	6.1	9.1	17.9	46.2
San Diego	32.7	10.4	3.7	6.1	16.0	36.2

time cold air outbreaks occur in the western North Atlantic or in the East China Sea, trajectories may cross regions of very intense sea surface temperature gradients associated with the Gulf Stream or the Kuroshio Current as was shown above. In Experiment 6 (Fig. 12) we attempt to simulate such air mass transformation by imposing the sea surface temperature field given by (1.1).

Fig. 12a reveals the remarkable deepening of the mixed layer predicted by the model. The predicted deepening agrees reasonably well with the observed deepening (Fig. 6a). Since h_M (Fig. 12b) increases while $(q + l)_M$ (Fig. 12c) remains nearly unchanged, the cloud-base height z_C increases. The turbulent fluxes (Figs. 12d–12f) are very large by eastern ocean standards. As might be expected there is a tendency for the largest fluxes to occur just after the largest sea surface temperature gradient is encountered. Note that at about 1750 km the $\rho\overline{(w'h')_S}$ and $\rho L\overline{(w'q')_S}$ curves cross, i.e., the sign of the air-sea temperature difference changes. Thus, the mixed-layer temperature has warmed up to the sea surface temperature while the mixed-layer moisture has changed little. This will be discussed further in the next section. Also shown in Fig. 12d are time- and space-averaged surface fluxes (Agee and Howley, 1977) for the AMTEX area during a cold outbreak period of AMTEX 74. It can be seen that the model results are of the same magnitude as the observations, even though we have used an idealized cold air outbreak situation. This indicates that the model is applicable to a wide range of advective situations.

6. Approximate analytic solutions

In this section we shall derive approximate analytic solutions to the governing equations. Assuming that w_B is given by $-Dz_B$, we can eliminate $\overline{(w'h')_S}$ and $\overline{(w'h')_B}$ from (3.1), (3.3) and (3.5) of Part I to obtain

$$\frac{dh_M}{dt} + \left(\frac{C_T V}{z_B} + D + \frac{1}{z_B}\frac{dz_B}{dt}\right)h_M = \frac{C_T V}{z_B}h_S^* + \left(D + \frac{1}{z_B}\frac{dz_B}{dt}\right)h_+ - \frac{F_+ - F_S}{z_B}. \quad (6.1)$$

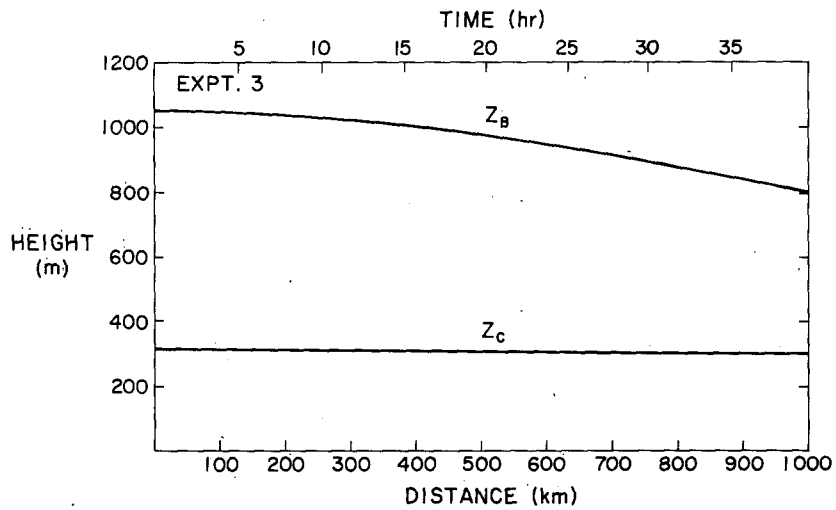

FIG. 9. Results for Experiment 3 (increasing divergence, constant sea surface temperature).

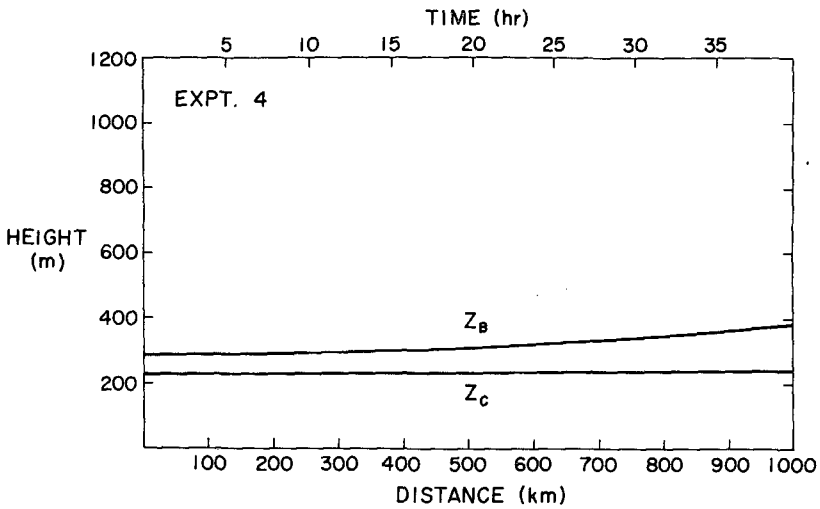

FIG. 10. Results for Experiment 4 (decreasing divergence, constant sea surface temperature).

Similarly, we can eliminate $\overline{(w'q')}_S$ and $\overline{w'(q' + l')}_B$ from (3.2), (3.4) and (3.6) of Part I to obtain

$$\frac{d(q + l)_M}{dt} + \left(\frac{C_T V}{z_B} + D + \frac{1}{z_B}\frac{dz_B}{dt}\right)(q + l)_M = \frac{C_T V}{z_B} q_S^* + \left(D + \frac{1}{z_B}\frac{dz_B}{dt}\right)q_+. \quad (6.2)$$

Eqs. (6.1) and (6.2) can be regarded as differential equations which give the variation of h_M and $(q + l)_M$ along the trajectory if the variations of z_B and $F_+ - F_S$ along the trajectory are known. The solutions to (6.1) and (6.2) are

$$h_M(t) = h_M(0) + \int_0^t a(t,t') \times \left\{\frac{C_T V(t')}{z_B(t')}[h_S^*(t') - h_M(0)] + \left[D(t') + \frac{1}{z_B(t')}\frac{dz_B}{dt'}\right][h_+(t') - h_M(0)] - \frac{F_+(t') - F_S(t')}{z_B(t')}\right\}dt', \quad (6.3)$$

and

$$(q + l)_M(t) = (q + l)_M(0) - \int_0^t a(t,t') \times \left\{\frac{C_T V(t')}{z_B(t')}[q_S^*(t') - (q + l)_M(0)] + \left[D(t') + \frac{1}{z_B(t')}\frac{dz_B}{dt'}\right] \times [q_+(t') - (q + l)_M(0)]\right\}dt', \quad (6.4)$$

where

$$a(t,t') = \exp\left\{-\int_{t'}^t \left[\frac{C_T V(t'')}{z_B(t'')} + D(t'') + \frac{1}{z_B(t'')}\frac{dz_B}{dt''}\right]dt''\right\}. \quad (6.5)$$

The solutions (6.3) and (6.4) show that the effects of upstream conditions are gradually forgotten as the result of the three terms in the integrand of (6.5), i.e., surface transfer ($C_T V/z_B$), entrainment due to mean subsidence (D), and entrainment due to boundary layer deepening in the downstream direction ($z_B^{-1}dz_B/dt$). The integrand of (6.5) is always positive since both $C_T V/z_B$ and $D + (z_B^{-1}dz_B/dt)$ (which is directly proportional to the net mass flow across the top of the mixed layer) are always positive. How fast are upstream conditions on h_M and $(q + l)_M$ forgotten? As an example let us consider Experiment 5. Even after the instantaneous sea surface temperature change, the quantities $C_T V/z_B$: D:$(z_B^{-1}dz_B/dt)$ do not vary much along the trajectory and have typical values of 28:4:2 in units of 10^{-6} s^{-1}. Thus, $a(t,t')$ can be roughly approximated by $\exp[-(C_T V/z_B)(t - t')]$, which is shown in Fig. 13. In this case it appears that, as far as h_M and $(q + l)_M$ are concerned, conditions more than 24 h upstream are more than 90% forgotten. As a second example let us consider Experiment 6. At 600–700 km the quantities $C_T V/z_B$:D:$z_B^{-1}(dz_B/dt)$ have the values 15:10:32 in units of 10^{-6} s^{-1}, while at 1600–1700 km they have the values 6:10:3. These figures are in sharp contrast to Experiment 5, indicating that the AMTEX situation is one in which mixing across cloud top plays a very important role. According to (6.3) this mixing across cloud top will tend to increase h_M, but according to (6.4) it will tend to de-

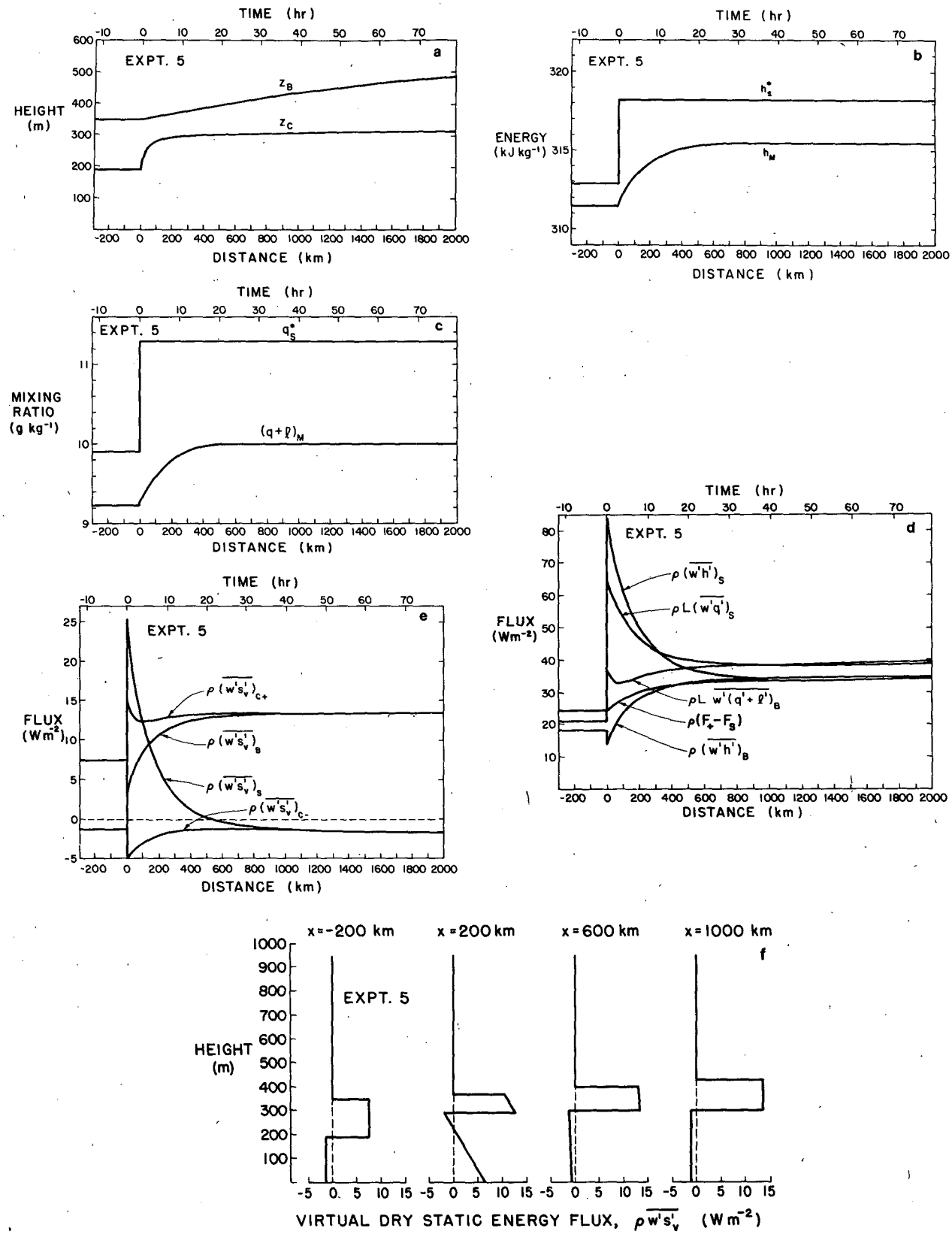

FIG. 11. Results for Experiment 5 (constant divergence, instantaneous 2°C increase in sea surface temperature).

crease $(q + l)_M$. Thus, in the AMTEX situation so much dry air is entrained across cloud top that the mixed layer does not moisten. However, the atmospheric column as a whole is rapidly moistening due to the increase in z_B. The relative magnitude of surface transfer to mixing across cloud top is measured by the important dimensionless quantity

$$\frac{C_T V}{Dz_B + \dfrac{dz_B}{dt}}.$$

For Experiment 5 this ratio is about 4 or 5, while for Experiment 6 it is about ⅓ or ½.

To determine the variation of z_B along the trajectory we could combine (3.3), (3.4), (3.5), (3.6), (3.10), (3.19), (3.28), (3.29) of Part I, and (6.3) and (6.4) of this section into a single differential equation for z_B. Although this can in principle be done, it leads to an extremely complicated equation for z_B. Here we shall consider only the minimum entrainment case and assume that the minimum $\overline{w's'_v}$ occurs at the surface.[1] The assumption that $(\overline{w's'_v})_S$ vanishes decouples the cloud base relation from the entrainment assumption, so that we have simply

$$h_M - (1 - \epsilon\delta)L(q + l)_M = s^*_{vS}. \tag{6.6}$$

Using (6.1), (6.2) and (6.6) we can easily obtain

$$\frac{dz_B}{dt} + \left\{D - \frac{1}{[s_{v+} - s^*_{vS}]}\frac{ds^*_{vS}}{dt}\right\}z_B = \frac{F_+ - F_S}{[s_{v+} - s^*_{vS}]}, \tag{6.7}$$

which is a differential equation for z_B provided $F_+ - F_S$ and s_{v+} are known. The solution of (6.7) is

$$z_B(t) = z_B(0) + \int_0^t b(t,t') \times \left\{\frac{1}{[s_{v+}(t') - s^*_{vS}(t')}\left[F_+(t') - F_S(t') + \frac{ds^*_{vS}}{dt'}\right] - D(t')z_B(0)\right\}dt', \tag{6.8}$$

where

$$b(t,t') = \exp\left\{-\int_{t'}^{t}\left[D(t'') - \frac{1}{s_{v+}(t'') - s^*_{vS}(t'')}\frac{ds^*_{vS}}{dt''}\right]dt''\right\}. \tag{6.9}$$

After the instantaneous sea surface temperature change of Experiment 5, ds^*_{vS}/dt is zero so that $b(t,t')$ can be written $\exp[-D(t - t')]$, which is also shown in Fig. 13. Since $C_T V/Dz_B$ for Experiment 5 is about 7, the memory time for z_B is about seven times the memory time for h_M and $(q + l)_M$.

Although we have derived (6.7)–(6.9) using the assumption that $(\overline{w's'_v})_S$ vanishes, our experience with numerical solutions indicates that the longer adjustment time for z_B compared to h_M and $(q + l)_M$ is a general feature, at least under typical eastern ocean situations.

7. Summary and conclusions

We have obtained both numerical and analytical solutions to the horizontally inhomogeneous version of a slightly generalized form of Lilly's (1968) cloud-topped mixed-layer model. The particular cases were chosen to illustrate boundary layer behavior as air flows through regions of varying sea surface temperature and large-scale divergence.

When boundary-layer air flows through a region of constant large-scale divergence and increasing sea surface temperature, the boundary layer warms, moistens and deepens in time, while the turbulent fluxes increase. In contrast, when air flows through a region of constant large-scale divergence and decreasing sea surface temperature, the boundary layer cools, dries and becomes shallower, while the turbulent fluxes decrease. In addition the cloud base descends and there is a tendency to form a surface fog.

When boundary layer air flows through regions of constant sea surface temperature but increasing or decreasing large-scale divergence, essentially no model variable changes except cloud top. Cloud top slowly rises if divergence is decreasing and slowly falls if divergence is increasing. Since the adjustment time for cloud top is long, the boundary layer depth may be far from its horizontally homogeneous steady-state value.

When wintertime cold air outbreaks occur over the warm boundary currents of the western oceans, very large surface fluxes and rapid boundary layer deepening occur. Although the surface evaporation can be very large, the boundary layer can deepen so rapidly in the downstream direction that mixing of dry air across cloud top maintains a relatively dry boundary layer.

Analytical solutions of the model reveal that

$$\frac{C_T V}{Dz_B + \dfrac{dz_B}{dt}}$$

is an important dimensionless quantity which measures the relative importance of surface transfer and mixing across cloud top. For typical eastern ocean situations this ratio is about 4 or 5, indicating that thermodynamic changes in the boundary layer are dominated by surface transfer. In AMTEX type

[1] The minimum occurs at the surface in Experiments 2, 3 and 4.

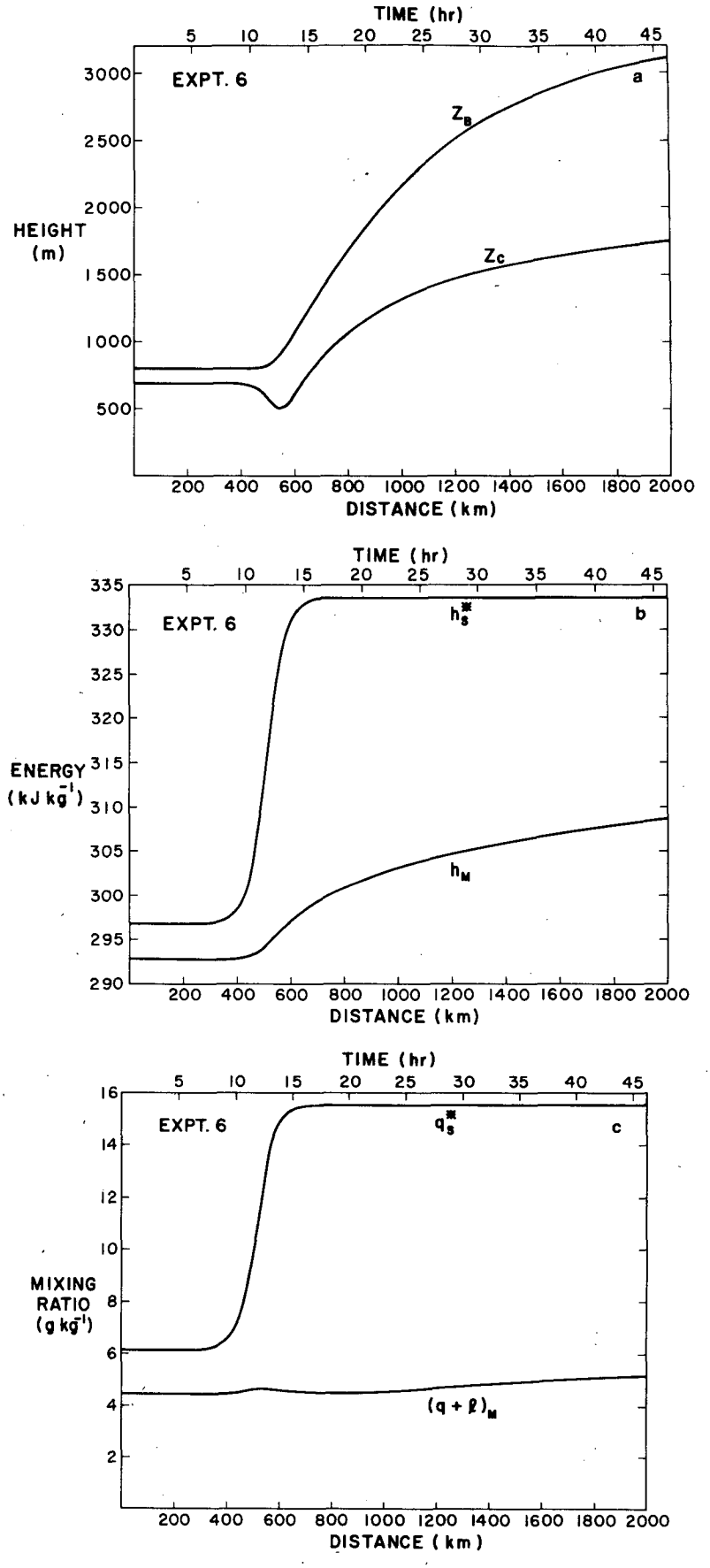

FIG. 12. Results for Experiment 6 (constant divergence, temperature rapidly increasing from 7 to 21°C). The horizontal lines included in Fig. 12d are AMTEX observations from Agee and Howley (1977).

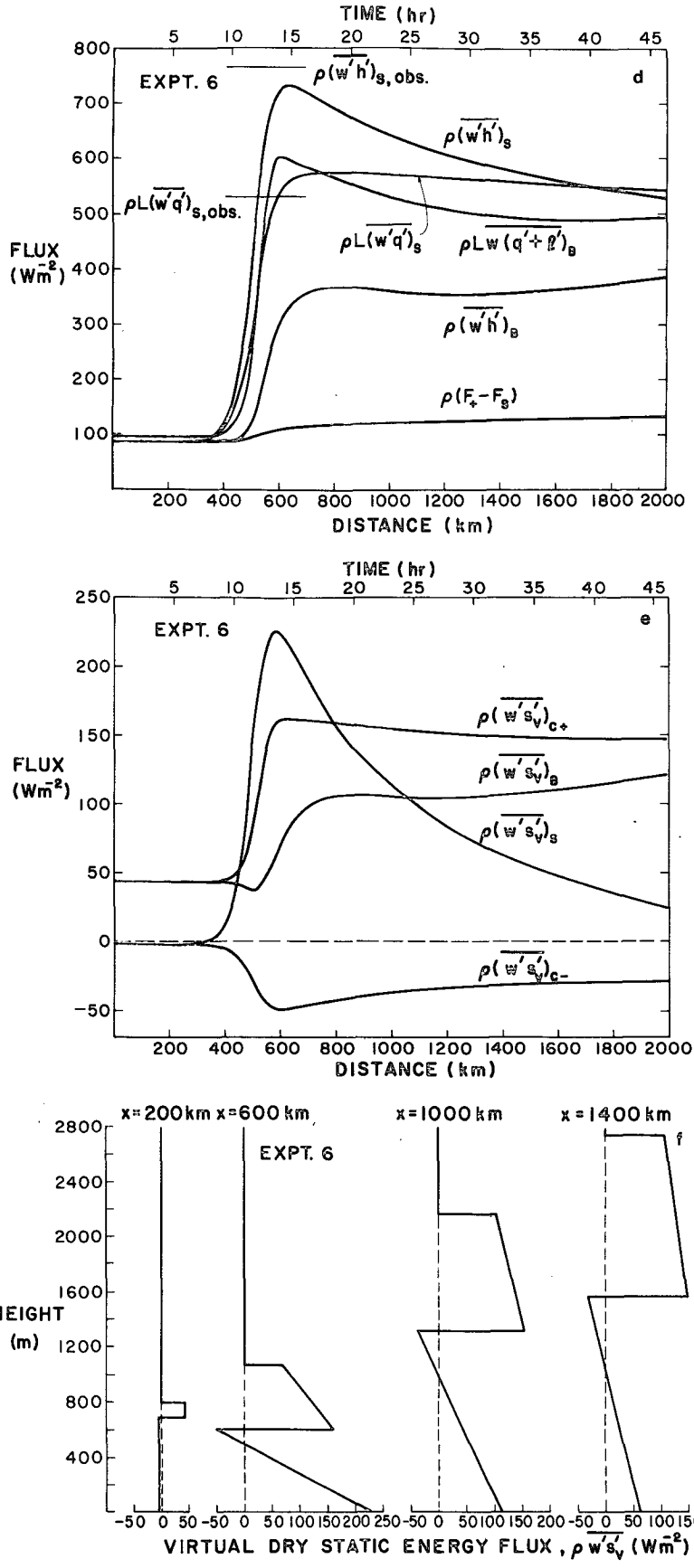

FIG. 12. (*Continued*)

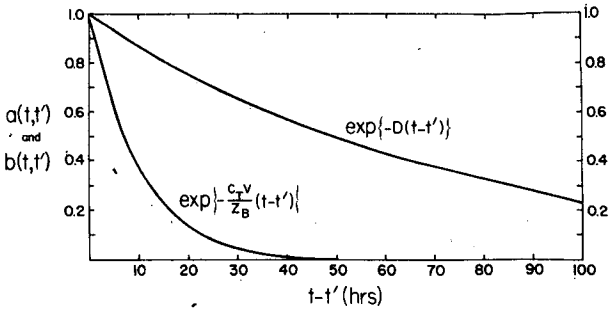

FIG. 13. The functions $\exp[-(C_T V/z_B)(t - t')]$ and $\exp \times [-D(t - t')]$ as approximations to $a(t,t')$ and $b(t,t')$, respectively. The curves are based on Experiments 5, in which $C_T = 0.0015$, $V = 7$ m s^{-1}, $D = 4 \times 10^{-6}$ s^{-1} and $z_B \approx 375$ m.

situations this ratio is about ⅓ or ½, indicating the dominance of mixing across cloud top.

Although the present theory seems capable of describing both eastern ocean stratocumulus and western ocean air mass transformation, there is still considerable room for generalizing the model. One possibility for generalization is to include the momentum budget so that surface winds and divergence are no longer externally specified but are dependent variables of the model. One might then specify only the sea surface temperature and pressure fields. Another possibility is to generalize the model to include both stratocumulus and trade cumulus convection. Then trajectories could be followed closer to the ITCZ, and one could study the transition from stratocumulus to trade cumulus convection. Such a model has recently been developed by Albrecht *et al.* (1979) along lines first proposed by Betts (1973).

Acknowledgments. We have benefited greatly from the comments of many colleagues including B. Albrecht, A. Arakawa, A. K. Betts, J. W. Deardorff, J. Hack, D. Lenschow, D. K. Lilly and P. Silva Dias. We are also indebted to Dorothy Chapman for her help in preparing this paper. The research reported here has been supported by the GARP Section of the Office of Climate Dynamics, National Science Foundation, under Grants ATM 76-09370 and OCD 74-21678.

REFERENCES

Agee, E. M., and R. P. Howley, 1977: Latent and sensible heat flux calculations at the air-sea interface during AMTEX 74. *J. Appl. Meteor.*, **16**, 443–447.

Albrecht, B. A., A. K. Betts, W. H. Schubert and S. K. Cox, 1979: A model of the thermodynamic structure of the trade-wind boundary layer: Part I. Theoretical formulation and sensitivity tests. *J. Atmos. Sci.*, **36**, 73–89.

Betts, A. K., 1973: Nonprecipitating cumulus convection and its parameterization. *Quart. J. Roy. Meteor. Soc.*, **99**, 178–196.

Cox, S. K., 1973: Infrared heating calculations with a water vapor pressure broadened continuum. *Quart. J. Roy. Meteor. Soc.*, **99**, 669–679.

Japanese Oceanographic Group, 1975: Outline of oceanographic conditions in AMTEX '74 and AMTEX '75. Sci. Rep. Fourth AMTEX Study Conference, AMTEX Rep. No. 8.

Lenschow, D. H., 1972: The Air Mass Transformation Experiment (AMTEX). *Bull. Amer. Meteor. Soc.*, **53**, 353–357.

——, and E. M. Agee, 1976: Preliminary results from the Air Mass Transformation Experiment (AMTEX). *Bull. Amer. Meteor. Soc.*, **57**, 1346–1355.

Lilly, D. K., 1968: Models of cloud-topped mixed layers under a strong inversion. *Quart. J. Roy. Meteor. Soc.*, **94**, 292–309.

Miller, F. R., and M. R. Stevenson, 1974: Comparison of cloud top temperatures from satellites and sea surface temperatures along Baja California. Paper presented at V Congreso Nacional de Oceanografia, October 1974. [Available from the authors at Scripps Institution of Oceanography].

Neiburger, M., D. S. Johnson and C. W. Chien, 1961: Studies of the structure of the atmosphere over the Eastern Pacific Ocean in summer, I: The inversion over the Eastern North Pacific Ocean. *Univ. Calif. Publ. Meteor.*, **1**, No. 1.

Ninomiya, K., 1976: Note on synoptic situation of AMTEX '75. *J. Meteor. Soc. Japan*, **54**, 334–337.

Schubert, W. H., J. S. Wakefield, E. J. Steiner and S. K. Cox, 1979: Marine stratocumulus convection, Part I: Governing equations and horizontally homogeneous solutions. *J. Atmos. Sci.*, **36**, 1286–1307.

U. S. Naval Weather Service, 1969: World-wide airfield summaries. Volume VIII, Part I. [NTIS AD 688 472].